Measurement of dc and ac Electric Fields inside an Atomic Vapor Cell with Wall-Integrated Electrodes

Lu Ma,[1,*,†] Michael A. Viray,[1,‡] David A. Anderson,[2] and Georg Raithel[1]

[1] *Department of Physics, University of Michigan, Ann Arbor, Michigan 48109, USA*

[2] *Rydberg Technologies Inc, Ann Arbor, Michigan 48103, USA*

(Received 5 December 2021; revised 8 May 2022; accepted 22 June 2022; published 1 August 2022)

We present and characterize a Rb atomic vapor cell with silicon-ring electrodes embedded between borosilicate glass tubes. The ring electrodes can be externally connectorized for application of electric fields to the inside of the cell. An atom-based, all-optical, laser-spectroscopic field-sensing method is employed to measure electric fields in the cell. Here, the Stark effect of electric-field-sensitive rubidium Rydberg atoms is exploited to measure dc electric fields in the cell of approximately 5 V/cm, with a relative uncertainty of 10%. Measurement results are compared with dc field calculations, allowing us to quantify electric field attenuation due to free surface charges inside the cell. We further measure the propagation of microwave fields into the cell, using Autler-Townes splitting of Rydberg levels as a field probe. Results are obtained for a range of microwave powers and polarization angles relative to the cell's ring electrodes. We compare the results with microwave-field calculations.

DOI: 10.1103/PhysRevApplied.18.024001

I. INTRODUCTION

The introduction of dc and ac electric fields into vapor-cell-based quantum devices currently is of considerable interest [1,2]. For instance, dc Stark tuning of Rydberg transition frequencies broadens the frequency range of Rydberg-atom-based microwave-field detectors [3–7]. Auxiliary rf fields for heterodyne rf field sensing in vapor-cell devices enhance sensitivity [8] and allow rf phase sensing [9–11]. Further, a range of quantum devices that require accurate control of in-vacuum electric fields could, potentially, be implemented inside miniaturized glass cells. These include Paul [12,13], Penning [14–16], and cusp [17] traps for ions, electrons and plasmas, and Faraday-shielded magneto-optical traps (MOTs) [18,19] for applications requiring controlled electromagnetic boundary conditions or a well-defined black-body radiation environment [20–22].

Atomic vapor cells with integrated materials and structures to generate and condition electromagnetic fields in atomic vapors provide a platform for compact quantum electromagnetic field sensors and devices [11,23,24]. dc and low-frequency electric field control inside glass vacuum cells using electrodes placed outside of the cells is challenging due to cell-internal photoelectric charging effects [25,26]. In Ref. [27], a dc-field shielding factor of 10^4 was measured, rendering cell-external electrodes generally incapable of generating useful cell-internal dc electric fields. While cell-internal photoelectric charging effects can be employed in a manner to enable electrode-free all-optical generation of cell-internal electric fields [28], physical electrodes inside the cell provide improved electric field control with greater flexibility in field geometry [29,30].

Here, we investigate a cell structure with conducting silicon electrodes integrated into the glass cell wall. The 5-mm-diameter and 35-mm-long cell, shown in Fig. 1(a), is fabricated using an anodic bonding [31–34] method and is filled with a buffer-gas-free natural Rb vapor. The cell features eight evenly spaced Si-ring electrodes along the length of the body. Application of different voltage combinations to the electrodes allows the realization of a variety of electric field geometries. The array of rings also serves as a partial polarizer for microwave radiation, due to the periodic 5-mm spacing between them. The cell has been devised as a stepping stone towards small Penning and other charged-particle traps that require inhomogeneous dc electric fields with quadrupolar components, as well as an ability to inject rf electric fields for charged-particle manipulation. These aspects of the cell structure are investigated in the present work.

We utilize laser spectroscopy of an atomic vapor to analyze the electric fields in the cell. This technique uses

*lukema@umich.edu

†Present address: Applied Materials, Inc., Santa Clara, California 95054, USA.

‡Present address: Georgia Tech Research Institute, Atlanta, Georgia 30318, USA.

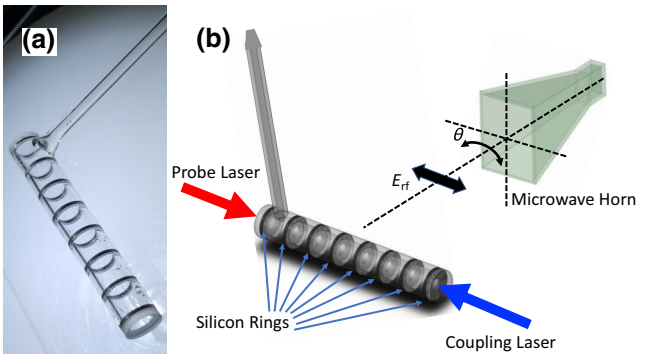

FIG. 1. Images of glass vapor cell with wall-integrated electrodes for application of dc and ac electric fields. (a) Picture of the cell. The black rings are conducting-Si rings. (b) Illustration of the testing setup, showing the cell, the ^{85}Rb $5S_{1/2} \rightarrow 5P_{3/2}$ EIT probe laser (780 nm, red), the $5P_{3/2} \rightarrow$ Rydberg EIT coupler laser (480 nm, blue), and the microwave-emitting horn. The lead wires to the Si rings are only connected for dc field measurements. The setup allows variation of the microwave polarization angle θ. The displayed case is for maximum microwave transmission into the cell.

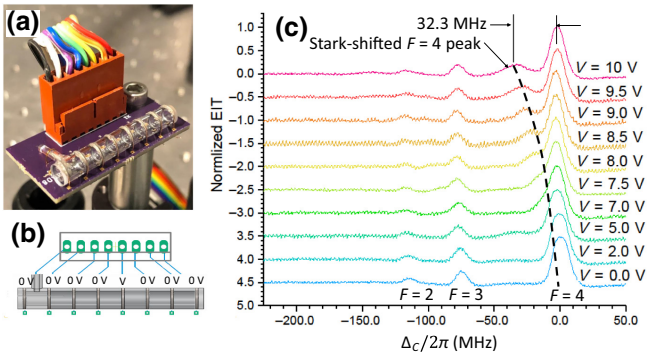

FIG. 2. (a) Picture of the cell setup used for spectroscopic dc electric field measurement in the cell. Individual voltages are applied to the conductive Si-ring electrodes through the ribbon cable and thin wires glued to the outer rims of the Si rings with conductive glue. (b) Wiring diagram used for the data in (c). (c) Rydberg-EIT spectra of Rb $31S_{1/2}$ for the indicated voltages V versus detuning of the coupler laser from the $5P_{3/2}$, $F = 4 \rightarrow 32S_{1/2}$ transition. The Stark-shifted peak, most clearly visible on the main line near 0 MHz, is due to quadratic dc Stark shifts near the voltage-carrying Si ring.

atoms in Rydberg states (states with high principal quantum number n) as electric (E) field probes. Though electromagnetically induced transparency (EIT) [35,36], the atoms yield narrow laser-spectroscopic lines that mark the optical excitation energy of the Rydberg levels. Rydberg-level Stark shifts can be observed via EIT line shifts. From measured line shifts and splittings one can determine the strength of the E field in the laser-probe region [7]. This technique, which takes advantage of the large susceptibilities of Rydberg atoms to dc and ac electric fields [37,38], has previously been used to observe a variety of electric fields, including radio HF and VHF fields [27,39,40], monochromatic [3–6] or modulated [41] microwave radiation, plasma electric fields [42,43], and dc electric fields [28,39,44].

We first study a dc electric field configuration by applying a variable dc voltage to one of the Si-ring electrodes, with the others grounded. In the second configuration, a microwave field is injected into the cell by radiating microwaves of variable intensity and polarization from a microwave horn into the cell. In each configuration, we analyze Rydberg-EIT signals to deduce the electric field.

II. EXPERIMENTAL SETUP

A. Optical and Electric Field Setup

Figure 1(b) shows the optical and microwave and dc electric field setup. We use a two-photon EIT ladder configuration in which the uppermost state is a Rydberg level. The two counterpropagating EIT lasers are overlapped along the cell axis, as illustrated in Fig. 1 (b). The first laser drives the ^{85}Rb $5S_{1/2} \rightarrow 5P_{3/2}$ EIT probe transition and has a wavelength of $\lambda_p = 780$ nm (red), a power of 11 μW, and a diameter of $w_0 = 464$ μm. The second laser (EIT coupler), runs at $\lambda_c = 480$ nm (blue) and 46 mW, has a diameter of $w_0 = 268$ μm, and drives the $5P_{3/2} \rightarrow 49D_{5/2}$ (ac field measurements) or the $5P_{3/2} \rightarrow 32S_{1/2}$ (dc field measurements) Rydberg transitions. The polarizations of the probe and coupler lasers are linear and parallel. The EIT signal is obtained by scanning the coupler laser across the Rydberg resonances. The probe beam is sent into a photodiode connected to a transimpedance amplifier. The EIT signal, displayed on and acquired with an oscilloscope, exhibits Rydberg transitions whose quadratic dc and linear ac Stark effects reveal the electric fields present in the cell.

The dc electric fields are applied by mounting the cell on a small piece of circuit board and connectorizing the Si rings to external voltage-control lines, as shown in some detail in Figs. 2(a) and 2(b).

In the microwave measurements, the vapor cell is mounted stem down on a thin acetal rod, which is held in place by a post holder. The Si rings are floating, with no wires attached. The microwave radiation is emitted from a 15-dBi standard gain microwave horn (Pasternack PE9852/2F-15) connected to a synthesizer. We set the microwave frequency to 18.149805 GHz to resonantly drive the $49D_{5/2} \rightarrow 50P_{3/2}$ Rydberg transition. The horn is attached to a rotating mount to allow for a variation of the microwave polarization angle θ [see Fig. 1(b)] over a range of 360°, with a resolution of 1°. The microwaves are incident onto the vapor cell at a right angle relative to the cell's axis, and the cell is located in the horn's far field, at a distance of 15 cm.

III. EXPERIMENTAL ANALYSIS

A. dc electric field

First, we test our device for dc electric field injection capability using the cell setup shown in Fig. 2(a). The strength of the dc field inside the cell is monitored through the dc Stark shift of the Rydberg EIT signal. In this test, the $32S_{1/2}$ Rydberg state, which has a dc polarizability α of 2.214 MHz/(V/cm)^2, is used. The quadratic Stark shift in a dc field $E_{\rm dc}$ is given by $-\alpha E_{\rm dc}^2/2$.

In Fig. 2(c) we show EIT scans versus coupler-laser frequency detuning, Δ_C, for a range of voltages V on the center Si ring, with all other rings grounded, as seen in Fig. 2(b). Considering first the $V = 0$ case, we note that there are three copies of the $32S_{1/2}$ EIT line near $\Delta_C = 0$ MHz, -75 MHz, and -115 MHz. The three copies belong to the $F = 4$, $F = 3$, and $F = 2$ hyperfine states of the intermediate $5P_{3/2}$ level, respectively. The observed hyperfine splittings are reduced by a factor $\lambda_p/\lambda_c - 1$ relative to the actual hyperfine splittings due to EIT Doppler shifts in the cell. The field-free EIT lines have a line width on the order of 15 MHz, mostly limited by our coupler- and probe-laser intensities that result in coupler and probe Rabi frequencies $\lesssim 10$ MHz.

When the voltage V applied to the center Si ring is increased [Fig. 2(b)], the EIT lines first develop shoulders in their lower-frequency wings, and at voltages above about 9 V a dc-field-shifted line separates from the field-free lines. This behavior is observed most clearly on the strongest ($F = 4$) resonance. On the weaker $F = 3$ EIT resonance, the dc-field-induced features are only marginally observable, due to low overall signal on that resonance, and on the weakest ($F = 2$) EIT resonance the dc-field-induced features are not observable. The shifted peaks arise from the quadratic dc-Stark effect of the $32S_{1/2}$ Rydberg level in the region around the center Si ring, where the applied voltage V induces dc electric fields. The maximum frequency separation between the dc-Stark-shifted $F = 4$ peak in Fig. 2(c) and the field-free $F = 4$ peak is (32.3 ± 5) MHz, corresponding to a measured dc electric field maximum of $E_{\rm dc} = (5.4 \pm 0.5)$ V/cm.

Most of the cell volume remains essentially field-free even at large V, as all Si rings except the one at the center are held on ground potential. Hence, the unshifted EIT resonances remain dominant in all spectra in Fig. 2(c). The line widths of the unshifted lines remain constant throughout, whereas the Stark-shifted lines broaden with increasing field due to dc-electric-field inhomogeneity. In the following paragraphs, we discus the detailed line shape based on electric field models for the cell.

In an initial step to interpret the EIT lines observed in Fig. 2(c), we compute the dc electric field, $E_{\rm dc}$, within the cell using a three-dimensional field simulation for the case where there are no surface charges on the dielectric glass walls. In this computation, we enter boundary conditions as shown in Fig. 2(b) for $V = 10$ V on the central SI ring, with proper dielectric constants throughout. The field along the cell's axis, shown in Fig. 3 (a), reflects the quadruplar structure of the field centered at the SI ring held at $V = 10$ V. From the computed electric field map, we then find the probability distribution, $P(E_{\rm dc})$, of the field within the probe region of our spectroscopic electric field measurement. In a separate calculation, which is based on the Lindblad equation for the density operator of the utilized EIT system, we simulate the EIT spectrum for the Stark-shift-free EIT line of the Rb $32S_{1/2}$-level, $S_0(\Delta_C)$, which is symmetric about and centered at $\Delta_C = 0$. The inhomogeneously dc-Stark-shifted and -broadened EIT spectrum, $S(\Delta_C)$, then follows from the convolution

$$S(\Delta_C) = \int S_0(\Delta_C + x)\left[P\left(\left|\frac{x}{\pi\alpha}\right|\right)/\sqrt{4\pi\,|\alpha x|}\right]dx, \quad (1)$$

where the magnitude of the Stark shift, x, is in units rad/s. This initial calculation produces EIT lines with quadratic Stark shifts that are about a factor of 10 larger than measured, corresponding to a factor of about 3 in electric field.

The fact that the dc electric field measured by Rydberg-EIT spectroscopy is almost a factor of 3 smaller than the simulated field suggests that the boundary conditions in our field simulation are incomplete. In view of the literature cited in the introduction, it is apparent that surface charges on the nonconducting inner glass surfaces of the cell reduce the cell-internal dc electric field. In an intermediate, heuristic step, we therefore apply a global attenuation of a factor of approximately equal to 3 to $E_{\rm dc}$, as visualized in Fig. 3(b). This results in a simulated spectrum [red line in Fig. 3(c)] that closely resembles the measured one (black line).

In light of this finding, in the final step of our spectroscopic modeling we then calculate the $E_{\rm dc}$ distribution for a physically realistic model in which the voltage-carrying Si ring is straddled by two grounded rings [orange sheaths in Fig. 3(e)] on the inner cell wall. The grounded rings simulate the field-reducing effect of surface charges accumulated on the inner glass surfaces near the voltage-carrying Si ring. The resultant simulated spectrum in Fig. 3(f) (red line) closely approaches the measured spectrum (black line), without any additional field attenuation needed to achieve agreement.

The electrode structure as well as the overall symmetry of the cell suggest that $E_{\rm dc}$ should have a leading quadrupole term, as is also evident in the field simulations. This electric field geometry is required for confining charged particles in Paul, Penning, and cusp traps. The results in Figs. 2 and 3 are consistent with the presence of such a field in the cell, albeit reduced by about a factor

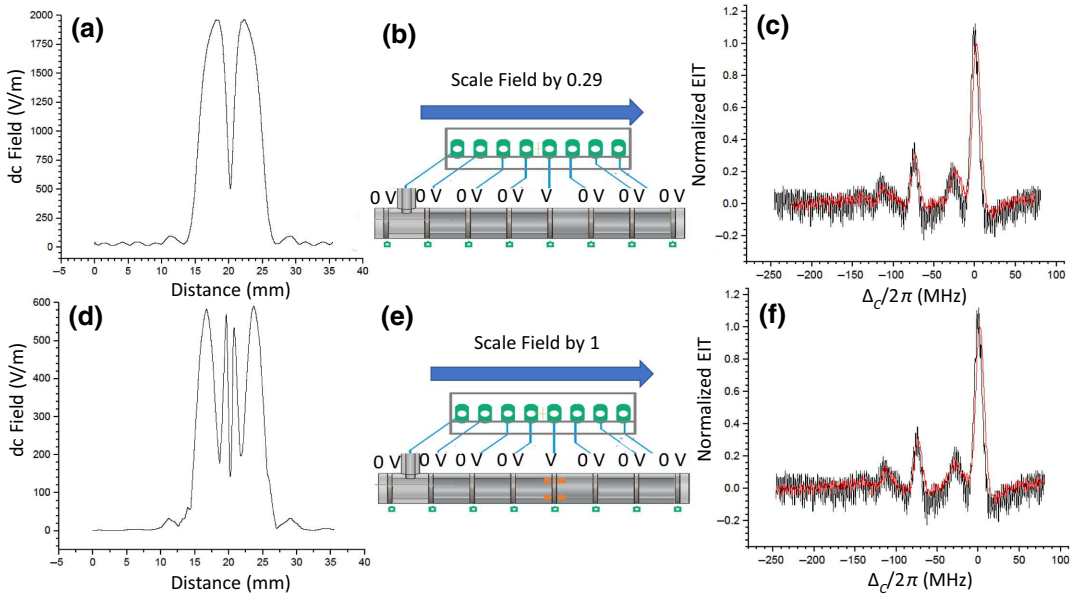

FIG. 3. Calculated dc electric fields for an unattenuated (a) and an attenuated (d) case for $V = 10$ V. Simulated dc Stark spectra are plotted in red in (c),(f), respectively, measured spectra are plotted in black. The calculated unattenuated dc field from (a) must be scaled down by a factor of approximately equal to 3, as visualized in (b), to arrive at a reasonable match between simulated and measured spectra in (c). In (d), the field is computed for a physically realistic scenario in which two grounded sheaths [orange parts in (e)] on both sides of the voltage-carrying Si ring emulate the effect of a field-reducing buildup of free charges, causing a field reduction. This model leads to reasonable agreement between simulated and measured spectra (f), without additional artificial field attenuation. The details of the field attenuation effects are discussed in Sec. III A.

of 3 from a surface-charge-free situation. Future spatially resolved Rydberg-EIT dc electric field measurements near the voltage-carrying SI ring may reveal more detail as to how exactly the field reduction by a factor of about 3 occurs. With this input, an improved physical model with refined boundary conditions could be developed. This research is beyond the scope of the present work.

B. Injected microwave electric fields

In the following, we study the propagation of a rf field of 16.5-mm wavelength into our cell with eight wall-integrated SI ring electrodes. The propagation is nontrivial because the cell dimensions (Si ring spacing 5 mm, overall cell length 35 mm, outer cell diameter 5 mm, inner cell diameter 3 mm) are on the order of the rf field's wavelength.

1. Varied Microwave Power at Fixed Polarization Angle

In a first set of microwave measurements, the horn is kept at $\theta = 0^\circ$ [see Fig. 1(b)], the microwave polarization angle of maximum transmission. The Si rings are on floating dc potentials and are not connected to any wires. We measure resonant Autler-Townes (AT) splittings of the $49D_{5/2} \rightarrow 50P_{3/2}$ Rydberg transition at 18.149805 GHz, for microwave powers injected into the horn of $P_{\text{horn}} =$ -3.7, -6.2, -9.0, -11.9, and -14.9 dBm, as measured by a power meter. Additionally, we record a control measurement where the microwave is turned off. In Fig. 4 we show the EIT spectra recorded at these values of P_{horn}. Since this measurement qualitatively differs from earlier work due to the presence of the Si rings, in the following we analyze the data in some detail.

In Fig. 5 we plot the AT splitting in MHz as a function of $\sqrt{P_{\text{horn}}/1\,\text{mW}}$. The black data points are the measured EIT-line splittings, denoted Δ_{meas}. The splittings are due to several effects. The microwave electric field, E_{MW}, induces an AT splitting that ideally is proportional to E_{MW} and that represents the dominant contribution to Δ_{meas} at the higher powers in Fig. 5. Further, Fig. 4 shows that there is a residual splitting of several MHz, denoted b, even when the microwave is turned off. The residual splitting is indicative of dc stray electric fields from the cell walls, and possibly a Zeeman splitting due to stray magnetic fields. We empirically quantify the splitting effects by applying a fit to the black (measured) data points of the form $\Delta_{\text{meas}} = \sqrt{(ax)^2 + b^2}$, where $x = \sqrt{P_{\text{horn}}/\text{mW}}$. The term ax accounts for the microwave-induced ideal AT splitting of the Rydberg line, which is dominant at higher microwave powers P_{horn}. The b term accounts for the stray-field-induced splitting, which is dominant at zero and low values of P_{horn}.

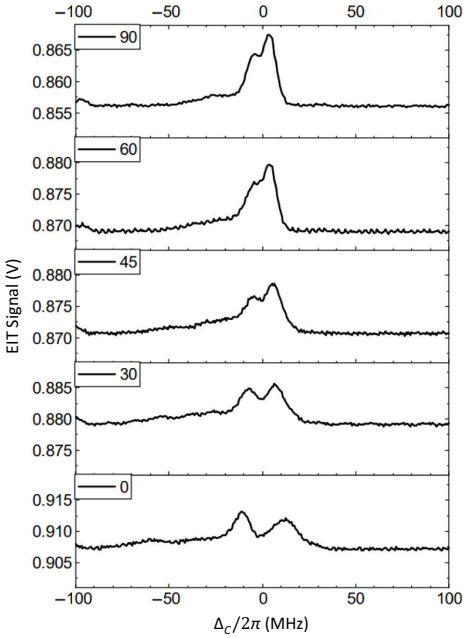

FIG. 4. EIT signals versus coupler laser detuning for the indicated microwave powers. For these data, the microwave polarization angle is set for maximum transmission ($\theta = 0$).

The fit result is shown in Fig. 5 in solid red. The a and b values from the fit are

$$a = (31.9 \pm 1.7)\ \text{MHz}/\sqrt{P_{\text{horn}}/\text{mW}},$$
$$b = (3.54 \pm 0.90)\ \text{MHz}. \tag{2}$$

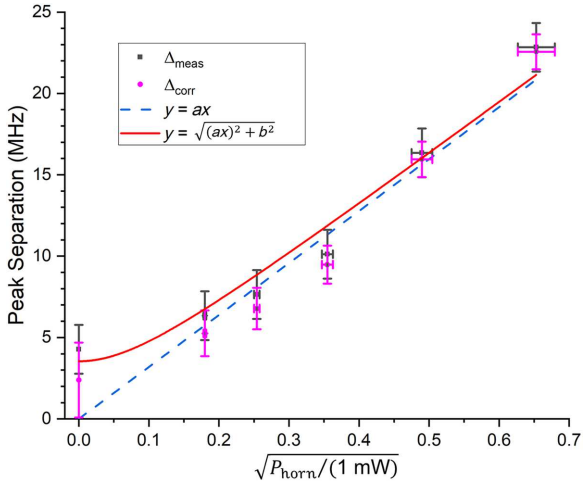

FIG. 5. Autler-Townes splitting of the EIT signal in MHz versus $x = \sqrt{P_{\text{horn}}/1\ \text{mW}}$. The black data points are measured peak separations, Δ_{meas}. The solid red curve is a fit for Δ_{meas} of the form $y = \sqrt{(ax)^2 + b^2}$ with fit parameters a and b [see Eq. (2)]. The dashed blue line shows $y = ax$. The magenta data points are corrected peak separations, Δ_{corr} [see Eq. (3)].

TABLE I. The columns show $x = \sqrt{P_{\text{horn}}/1\text{mW}}$, the measured splittings Δ_{meas}, the electric fields E_{MW} calculated from Eqs. (3) and (4), and the ratio x/E_{MW}, which should ideally be constant.

$\sqrt{P_{\text{horn}}/1\text{mW}}$	Δ_{meas} (MHz)	E_{MW} (V/m)	x/E_{MW} (m/V)
0.18 ± 0.01	6.3 ± 1.5	0.36 ± 0.09	0.50 ± 0.12
0.25 ± 0.01	7.7 ± 1.5	0.44 ± 0.09	0.58 ± 0.12
0.36 ± 0.01	10 ± 1.5	0.58 ± 0.09	0.62 ± 0.09
0.49 ± 0.02	16 ± 1.5	0.93 ± 0.09	0.53 ± 0.05
0.65 ± 0.02	23 ± 1.5	1.3 ± 0.09	0.50 ± 0.04

The dashed blue line in Fig. 5 shows the ideal microwave-induced AT splitting, ax, that the Rydberg line would exhibit in a Doppler-free cold-atom measurement [45] with no dc fields present. The magenta data points are corrected line splittings, Δ_{corr}, in which we subtract off the splitting contribution due to the dc stray field according to

$$\Delta_{\text{corr}} = \sqrt{\Delta_{\text{meas}}^2 - b^2} \approx ax. \tag{3}$$

The value of Δ_{corr} has an improved linear relationship with the microwave field E_{MW}.

The corrected splitting, Δ_{corr}, approximately equals the Rabi frequency, Ω_0, of the resonantly driven microwave transition (in Hz). The following equation applies:

$$E_{\text{MW}}d/h = \Omega_0 = ax \approx \Delta_{\text{corr}}. \tag{4}$$

Here, d is the transition dipole moment, and h is Planck's constant. Our applied microwave field drives the $49D_{5/2} \rightarrow 50P_{3/2}$ Rydberg transition, which has a known transition dipole moment of $d = 1.16 \times 10^{-26}$ Cm. Equation (4) and the corrected splittings Δ_{corr} then allow us to calculate the electric field E_{MW}.

A summary of results is shown in Table I. Overall, the data series shows that E_{MW} can be measured in our cell with wall-integrated Si electrodes using established methods for atom-based microwave electric field sensing [3–6,45]. The field injected into the cell is only about 60% of the field that would be present without the cell (see details in Sec. IV). In view of anticipated electron-, ion-, and plasma-trapping applications of this cell, here it mostly is useful to conclude that microwave field injection into the cell for plasma diagnostics and charged-particle-drive will be efficient. A detailed evaluation of the cell for the purpose of microwave field metrology is not part of the present study.

2. Varied polarization angle at fixed microwave power

In our second set of microwave measurements we use a fixed power $P_{\text{horn}} = -3.7$ dBm and the horn is rotated. We take measurements of the AT splitting from $\theta = 0°$ (maximum transmission) to $\theta = 90°$ (minimum transmission), going in increments of about 10°. In Fig. 6 we show the

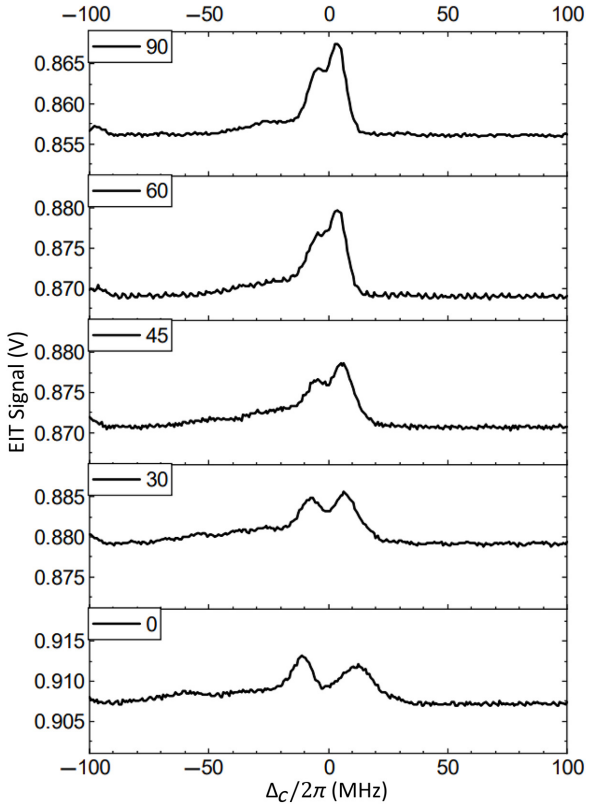

FIG. 6. EIT signals versus coupler-laser detuning for the indicated values θ of the incident microwave polarization. The power is fixed at $P_{\text{horn}} = -3.7$ dBm, the highest value in Fig. 5.

AT splitting of the EIT signal at selected angles, and in Fig. 7 the measured (black) and corrected (red) splittings in MHz for all angles. We see that, as expected, the splitting decreases as the polarization of the microwave-field direction becomes aligned parallel with the conducting rings.

It is instructive to compare the observed polarization dependence with that of an ideal microwave polarizer (such as the one formed by a large, planar grid of parallel wires with a wire separation much less than the microwave wavelength). The transmission behavior of the ideal microwave polarizer follows Malus' law [46], i.e., the transmitted electric field, E_{MW}, would be

$$E_{\text{MW}} = E_0 \cos(\theta). \tag{5}$$

There, E_0 is the field without polarizer, and the angle θ is defined such that maximum transmission occurs at $\theta = 0°$. For comparison, we add a blue, dashed curve in Fig. 7 that represents the behavior of an ideal microwave polarizer.

Comparing the measured and corrected separations, Δ_{meas} and Δ_{corr}, with the Malus-law curve, we see that the separations not only decrease faster with θ for $\theta \lesssim 30°$, but they also level out at about 25% of the $\theta = 0$ splitting when θ approaches 90°. Evidently, the cell electrodes

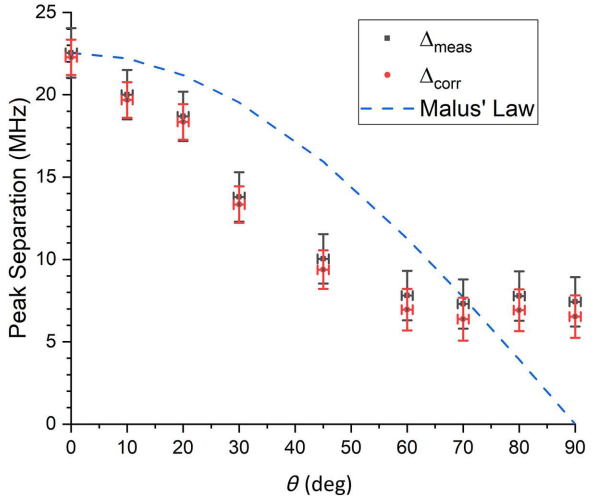

FIG. 7. Splittings Δ_{meas} (black) and Δ_{corr} (pink) versus polarization angle of the incident microwave radiation, with the relation between Δ_{meas} and Δ_{corr} established in Eq. (3). For reference, the dashed blue curve represents Malus' law, as it would apply for an ideal microwave polarizer.

do not act as a perfect microwave polarizer, as explained more in the following paragraph. In view of applications that require external microwave injection, the results show that the amplitude of microwave fields polarized transversely relative to the cell axis is about 30% of that of fields polarized parallel to the cell axis. This is relevant, for instance, if one intended to drive the electron cyclotron motion in a vapor-cell Penning trap formed with the cell. This trap would have a strong magnetic field along the cell axis, and the cyclotron motion would be transverse, requiring a transversely polarized ($\theta = 90°$) microwave field to drive it.

There are several reasons as to why the cell is not an ideal microwave polarizer. Mostly, the cell structure—finite conductive-Si rings embedded in a dielectric with large dielectric constant—exhibits a microwave response that differs substantially from that of a grid of parallel wires in vacuum. This is shown in the microwave-field simulations below. The simulations also bear out that the field polarization inside the cell may have some ellipticity. A minor effect that may contribute to the measurement result is that, while the microwave horn is perfectly polarized at our level of precision, reflections of microwaves from parts of the setup may be polarized differently from the incident wave and may enter into the cell. We can discard another potential cause for nonideal polarizer behavior, namely that the skin depth in the Si could, in principle, be too large. For the silicon we use, we estimate a skin depth $\lesssim 10$ μm at 18 GHz, which is 1/50 of the ring thickness. Hence, the Si rings behave as near-ideal conductors, as confirmed in our microwave simulations.

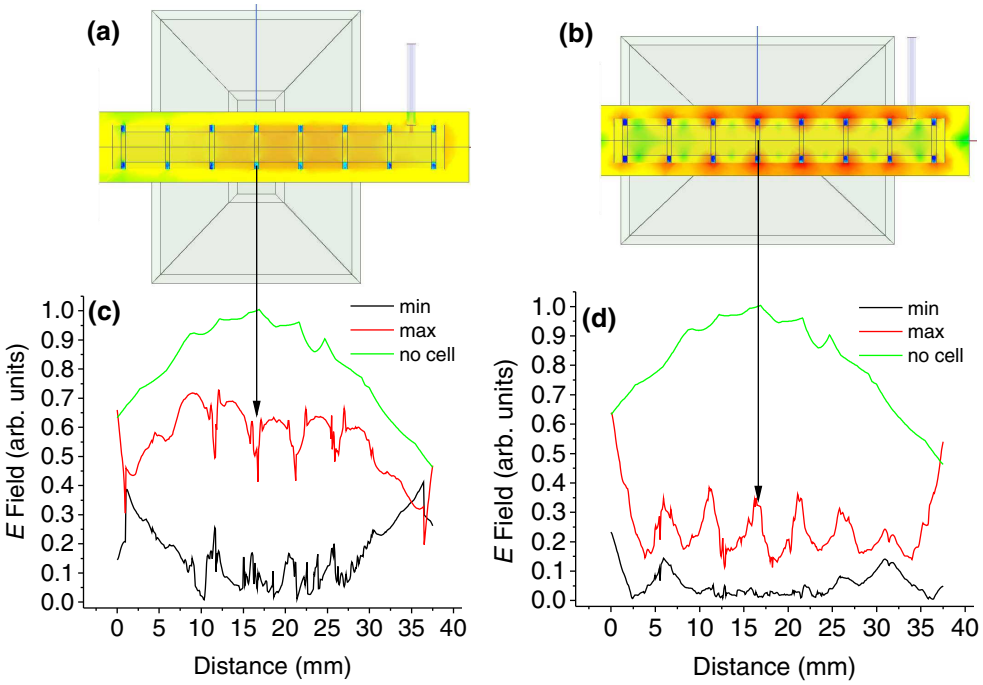

FIG. 8. Results of an Ansys HFSS simulation of the microwave experiment described in Sec. III B. (a),(b) Horn and cell geometries, as well as the calculated electric field distributions on planes containing the cell axis (colors explained in text). (c),(d) Field-strength magnitudes on the cell axis at temporal phases of maximal (red) and minimal (black) field strength, and for the case that the cell is absent (green).

IV. MICROWAVE SIMULATIONS

To gain more insight into the microwave experiment discussed in Sec. III B, we simulate the horn plus cell system using Ansys HFSS software for the geometric parameters used in the experiment. The model further uses accurate dielectric constants and resistivities. Here we show results for $\theta = 0^\circ$ and 90°. We also run simulations without the cell present to calibrate the in-cell microwave fields relative to the cell-free case.

Figures 8(a) and 8(b) show the geometries for $\theta = 0^\circ$ and 90°. The coloring inside the cell indicates the microwave electric field magnitude at the temporal phase when the field is greatest, on a color scale ranging from green (weak) to red (strong field). Figures 8(c) and 8(d) show the field magnitude along the cell axis at the temporal phases of maximal (red) and minimal (black) fields. The green curve shows the maximal field without cell present. (The field minimum without cell present is practically zero, because the incident field is linearly polarized.)

Since the experimental data represent an average of the microwave field along the length of the cell, we look at the behavior of the simulated-field averages. Figures 8(a) and 8(c) ($\theta = 0$, corresponding to largest transmission overall), show that the electric field transmission, averaged along the cell's axis, is about 60% of what it would be if no cell were present. Figures 8(b) and 8(d) ($\theta = 90^\circ$, corresponding to lowest transmission overall), indicate a transmission near 25% of what it would be if no cell were present. The simulated average-field ratio for the two cases therefore is about 2.5:1, whereas in the experiment it is about 3:1. We therefore see good qualitative agreement between the simulated and measured field ratios. Deviations are mostly attributed to fabrication uncertainties in the cell geometry.

While the experiment in its present form yields only a field average, the simulation has sub-mm spatial resolution. The electric field distributions in Figs. 8(a) and 8(c) show that for $\theta = 0^\circ$ (high transmission) the field tends to be larger in the spaces between the rings and weaker in the planes of the rings. For $\theta = 90^\circ$ [low transmission, Figs. 8(b) and 8(d)], the opposite trend is observed. Another noteworthy detail is that the field minima (black curves) are substantially larger than zero (5% to 10% of the cell-free field, in both cases of θ). This is indicative of a slightly elliptical character of the field's polarization inside the cell. The ellipticity is attributed to the fact that the cell components are neither infinitely long parallel wires, nor is the space between the rings filled by vacuum (as it would be for a parallel-wire microwave field polarizer). It is therefore plausible to assume that the structural parts scatter the field into directions orthogonal to the incident field, with material-related phase shifts. This can lead to elliptically

polarized net fields on the cell axis, as suggested by the black and red curves in Figs. 8(c) and 8(d).

V. CONCLUSION

We investigate a buffer-gas-free Rb vapor cell with conductive Si-ring electrodes integrated in the glass body. dc electric fields applied via the electrodes and microwave electric fields radiated into the cell from a horn antenna are measured using atomic field sensing methods. Measurement results are compared with simulations, and reasonable agreement is found. A remaining issue is how exactly does the observed reduction of the dc electric field by about a factor of 3 occur. Future position-resolved spectroscopic field measurements may be helpful to shed more light on the exact field-reduction mechanism. Cells with wall-integrated electrodes present opportunities in science and technology for realizing alternative types of Paul, Penning, and cusp traps.

ACKNOWLEDGMENTS

This work is supported by NSF Grants No. PHY-1707377 and No. PHY-1806809 and Rydberg Technologies Inc. We thank Dr. Pilar Herrera-Fierro and her team at the University of Michigan Lurie Nanofabrication Facility for their technical support, and Professor Tim Chupp and Dr. Skyler Degenkolb for helpful discussions. GR has an interest in Rydberg Technologies Inc, Ann Arbor.

[1] D. H. Meyer, P. D. Kunz, and K. C. Cox, Waveguide-Coupled Rydberg Spectrum Analyzer from 0 to 20 GHz, Phys. Rev. Appl. **15**, 014053 (2021).

[2] C. L. Holloway, N. Prajapati, J. Kitching, J. A. Sherman, C. Teale, A. Rufenacht, A. B. Artusio-Glimpse, M. T. Simons, A. K. Robinson, and E. B. Norrgard, Electromagnetically induced transparency based Rydberg-atom sensor for quantum voltage measurements, arXiv:2110.02335.

[3] J. A. Sedlacek, A. Schwettmann, H. Kübler, R. Löw, T. Pfau, and J. P. Shaffer, Microwave electrometry with Rydberg atoms in a vapour cell using bright atomic resonances, Nat. Phys. **8**, 819 (2012).

[4] J. A. Sedlacek, A. Schwettmann, H. Kübler, and J. P. Shaffer, Atom-Based Vector Microwave Electrometry using Rubidium Rydberg Atoms in a Vapor Cell, Phys. Rev. Lett. **111**, 063001 (2013).

[5] H. Q. Fan, S. Kumar, R. Daschner, H. Kübler, and J. P. Shaffer, Subwavelength microwave electric-field imaging using Rydberg atoms inside atomic vapor cells, Opt. Lett. **39**, 3030 (2014).

[6] C. L. Holloway, J. A. Gordon, S. Jefferts, A. Schwarzkopf, D. A. Anderson, S. A. Miller, N. Thaicharoen, and G. Raithel, Broadband Rydberg atom-based electric-field probe for Si-traceable, self-calibrated measurements, IEEE Trans. Antennas Propag. **62**, 6169 (2014).

[7] D. A. Anderson, G. Raithel, N. Thaicharoen, S. A. Miller, and A. Schwarzkopf, Atom-based electromagnetic radiation electric-field sensor (2018), US Patent US9970973B2.

[8] M. Jing, Y. Hu, J. Ma, H. Zhang, L. Zhang, L. Xiao, and S. Jia, Atomic superheterodyne receiver based on microwave-dressed Rydberg spectroscopy, Nat. Phys. **16**, 911 (2020).

[9] M. Simons, A. Haddab, J. Gordon, and C. Holloway, in *2019 International Symposium on Electromagnetic Compatibility - EMC EUROPE* (IEEE, Fort Lauderdale, FL, USA, 2019).

[10] D. Anderson, R. Sapiro, and G. Raithel, Rydberg atoms for radio-frequency communications and sensing: Atomic receivers for pulsed rf field and phase detection, IEEE Aerosp. Electron. Syst. Mag. **35**, 48 (2020).

[11] D. A. Anderson, G. Raithel, E. G. Paradis, and R. E. Sapiro, Atom-based electromagnetic field sensing element and measurement system (2020), US Patent US10823775B2.

[12] D. Leibfried, R. Blatt, C. Monroe, and D. Wineland, Quantum dynamics of single trapped ions, Rev. Mod. Phys. **75**, 281 (2003).

[13] K. Ito, T. Okano, K. Moriya, K. Fukushima, H. Higaki, and H. Okamoto, in *TCP 2014*, edited by M. Wada, P. Schury, and Y. Ichikawa (Springer International Publishing, Cham, 2017), p. 29.

[14] L. S. Brown and G. Gabrielse, Geonium theory: Physics of a single electron or ion in a penning trap, Rev. Mod. Phys. **58**, 233 (1986).

[15] D. Hall and G. Gabrielse, Electron Cooling of Protons in a Nested Penning Trap, Phys. Rev. Lett. **77**, 1962 (1996).

[16] B. J. McMahon, C. Volin, W. G. Rellergert, and B. C. Sawyer, Doppler-cooled ions in a compact reconfigurable penning trap, Phys. Rev. A **101**, 013408 (2020).

[17] Y. Enomoto *et al.*, Synthesis of Cold Antihydrogen in a Cusp Trap, Phys. Rev. Lett. **105**, 243401 (2010).

[18] K. Beloy, X. Zhang, W. F. McGrew, N. Hinkley, T. H. Yoon, D. Nicolodi, R. J. Fasano, S. A. Schäffer, R. C. Brown, and A. D. Ludlow, Faraday-Shielded dc Stark-Shift-Free Optical Lattice Clock, Phys. Rev. Lett. **120**, 183201 (2018).

[19] C. S. Nichols, L. M. Nofs, M. A. Viray, L. Ma, E. Paradis, and G. Raithel, Magneto-optical Trap with Millimeter Ball Lenses, Phys. Rev. Appl. **14**, 044013 (2020).

[20] I. Ushijima, M. Takamoto, M. Das, T. Ohkubo, and H. Katori, Cryogenic optical lattice clocks, Nat. Photonics **9**, 185 (2015).

[21] Y.-L. Xu and X.-Y. Xu, Analysis of the blackbody-radiation shift in an ytterbium optical lattice clock, Chin. Phys. B **25**, 103202 (2016).

[22] A. Golovizin, E. Fedorova, D. Tregubov, D. Sukachev, K. Khabarova, V. Sorokin, and N. Kolachevsky, Inner-shell clock transition in atomic thulium with a small blackbody radiation shift, Nat. Commun. **10**, 1724 (2019).

[23] D. A. Anderson, E. G. Paradis, and G. Raithel, A vapor-cell atomic sensor for radio-frequency field detection using a polarization-selective field enhancement resonator, Appl. Phys. Lett. **113**, 073501 (2018).

[24] E. Paradis, G. Raithel, and D. A. Anderson, Atomic measurements of high-intensity VHF-band radio-frequency fields with a Rydberg vapor-cell detector, Phys. Rev. A **100**, 013420 (2019).

[25] A. K. Mohapatra, T. R. Jackson, and C. S. Adams, Coherent Optical Detection of Highly Excited Rydberg States

using Electromagnetically Induced Transparency, Phys. Rev. Lett. **98**, 113003 (2007).
[26] Y.-Y. Jau and T. Carter, Vapor-Cell-Based Atomic Electrometry for Detection Frequencies below 1 KHz, Phys. Rev. Appl. **13**, 054034 (2020).
[27] S. Miller, D. Anderson, and G. Raithel, Radio-frequency-modulated Rydberg states in a vapor cell, New J. Phys. **18**, 053017 (8 pp.) (2016).
[28] L. Ma, E. Paradis, and G. Raithel, DC electric fields in electrode-free glass vapor cell by photoillumination, Opt. Express **28**, 3676 (2020).
[29] D. Barredo, H. Kübler, R. Daschner, R. Löw, and T. Pfau, Electrical Readout for Coherent Phenomena Involving Rydberg Atoms in Thermal Vapor Cells, Phys. Rev. Lett. **110**, 123002 (2013).
[30] R. Daschner, R. Ritter, H. Kübler, N. Frühauf, E. Kurz, R. Löw, and T. Pfau, Fabrication and characterization of an electrically contacted vapor cell, Opt. Lett. **37**, 2271 (2012).
[31] L. A. Liew, S. Knappe, J. Moreland, H. Robinson, L. Hollberg, and J. Kitching, Microfabricated alkali atom vapor cells, Appl. Phys. Lett. **84**, 2694 (2004).
[32] J. Kitching, Chip-scale atomic devices, Appl. Phys. Rev. **5**, 031302 (2018).
[33] H. Nishino, Y. Yano, M. Hara, M. Toda, M. Kajita, T. Ido, and T. Ono, Reflection-type vapor cell for micro atomic clocks using local anodic bonding of 45° mirrors, Opt. Lett. **46**, 2272 (2021).
[34] Y. Sebbag, E. Talker, A. Naiman, Y. Barash, and U. Levy, Demonstration of an integrated nanophotonic chip-scale alkali vapor magnetometer using inverse design, Light Sci. Appl. **10**, 54 (2021).
[35] M. Scully and M. Zubairy, *Quantum Optics* (Cambridge University Press, Cambridge, UK, 1997).
[36] M. Fleischhauer, A. Imamoglu, and J. P. Marangos, Electromagnetically induced transparency: Optics in coherent media, Rev. Mod. Phys. **77**, 633 (2005).
[37] R. Stebbings, F. Dunning, and F. Dunning, *Rydberg States of Atoms and Molecules* (Cambridge University Press, Cambridge, UK, 1983).
[38] T. Gallagher, *Rydberg Atoms* (Cambridge University Press, Cambridge, UK, 2005).
[39] M. G. Bason, M. Tanasittikosol, A. Sargsyan, A. K. Mohapatra, D. Sarkisyan, R. M. Potvliege, and C. S. Adams, Enhanced electric field sensitivity of rf-dressed rydberg dark states, New J. Phys. **12**, 065015 (2010).
[40] Y. Jiao, X. Han, Z. Yang, J. Li, G. Raithel, J. Zhao, and S. Jia, Spectroscopy of cesium rydberg atoms in strong radio-frequency fields, Phys. Rev. A **94**, 023832 (2016).
[41] D. A. Anderson, R. E. Sapiro, and G. Raithel, An atomic receiver for AM and FM radio communication, IEEE Trans. Antennas Propag. **69**, 2455 (2021).
[42] D. A. Anderson, G. Raithel, M. Simons, and C. L. Holloway, Quantum-optical spectroscopy for plasma electric field measurements and diagnostics, arXiv:1712.08717 [physics.atom-ph] (2017).
[43] D. Weller, J. P. Shaffer, T. Pfau, R. Löw, and H. Kübler, Interplay between thermal Rydberg gases and plasmas, Phys. Rev. A **99**, 043418 (2019).
[44] J. Grimmel, M. Mack, F. Karlewski, F. Jessen, M. Reinschmidt, N. Sandor, and J. Fortagh, Measurement and numerical calculation of Rubidium Rydberg Stark spectra, New J. Phys. **17**, 053005 (8 pp.) (2015).
[45] C. Holloway, M. Simons, J. Gordon, A. Dienstfrey, D. Anderson, and G. Raithel, Electric field metrology for SI traceability: Systematic measurement uncertainties in electromagnetically induced transparency in atomic vapor, J. Appl. Phys. **121**, 233106 (9 pp.) (2017).
[46] D. Halliday, R. Resnick, and J. Walker, *Fundamentals of Physics* (Wiley, Hoboken, 2008), 8th ed.